CrossMark

ORIGINAL PAPER: NANO-STRUCTURED MATERIALS (PARTICLES, FIBERS, COLLOIDS, COMPOSITES, ETC.)

Structural and magnetic phase transition of sol–gel-synthesized Cr$_2$O$_3$ and MnCr$_2$O$_4$ nanoparticles

Adnan Afzal[1] · Shahid Atiq[1] · Murtaza Saleem[2] · Shahid M. Ramay[3] ·
Shahzad Naseem[1] · Saadat A. Siddiqi[4]

Abstract Cr$_2$O$_3$ and MnCr$_2$O$_4$ spinel chromite nanoparticles were synthesized using chemically derived sol–gel technique. Crystal structure was analyzed using X-ray diffraction, and phase transition from a rhombohedral symmetry (R-3c) for Cr$_2$O$_3$ to a spinel cubic symmetry ($Fd3\,m$) for MnCr$_2$O$_4$ has been observed. Data obtained from diffraction were also utilized to evaluate the lattice parameters, crystallite size and unit cell volume. Micrographs obtained using a field emission scanning electron microscope exhibited well-shaped, homogenously distributed 30–70-nm-sized nanoparticles, with well-defined grain. Stoichiometric composition of all the elements present in the samples was confirmed using energy-dispersive X-ray spectroscopy. Dynamic light scattering measurement was performed to corroborate the hydrodynamic diameter and distribution of Cr$_2$O$_3$ and MnCr$_2$O$_4$ nanoparticles. The magnetic behavior of samples was scrutinized as a function of temperature and applied field. It was observed that Cr$_2$O$_3$ exhibited paramagnetic behavior both at room temperature and at 5 K, while a magnetic phase transition from ferro to para was observed in MnCr$_2$O$_4$ with a Curie temperature, $T_c \sim 50$ K.

Graphical Abstract
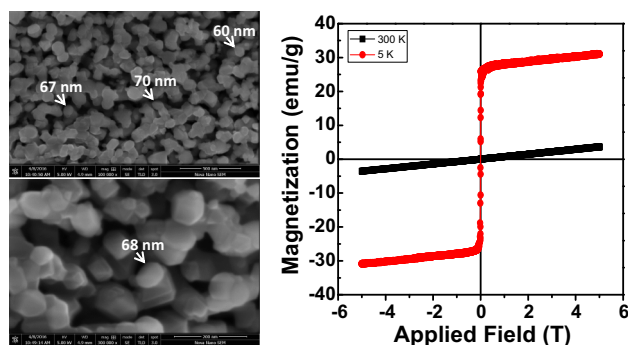
1 Introduction

Nanostructured spinel chromites have emerged as charming materials for potential use in many applications, for example in semiconductor devices, humidity sensors, photocatalysis, removal of impurity from weather and oxidation of chlorinated organic pollutants [1–5]. Owing to these gigantic applications, these materials are mostly studied in bulk form [6]. In the recent years, Cr$_2$O$_3$ clusters have also reaped attention due to their interesting magnetic properties at the nanolevel [7, 8]. Due to a wide range of applications in magnetic storage devices and electronics, etc., materials with such magnetic characteristics are quite exciting among the researchers worldwide. Addition of

✉ Shahid Atiq
satiq.cssp@pu.edu.pk

[1] Centre of Excellence in Solid State Physics, University of the Punjab, Lahore 54590, Pakistan

[2] Department of Physics, School of Sciences and Engineering (SSE), Lahore University of Management Sciences (LUMS), Lahore 54792, Pakistan

[3] Department of Physics and Astronomy, College of Science, King Saud University, P.O. Box 2455, Riyadh 11421, Saudi Arabia

[4] Interdisciplinary Research Centre in Biomedical Materials, COMSATS Institute of Information Technology, Lahore 54600, Pakistan

transition metal ions, such as Mn, Fe or Zn in Cr_2O_3, results in the structural transformation from one crystalline phase to another, which affects the structural morphology and hence the magnetic properties. For instance, Mn incorporation in Cr_2O_3 results in $MnCr_2O_4$ which behaves as a ferromagnetic material below room temperature (RT). One of the key focuses of the present day research on such chromites is to enhance the magnetic phase transition temperature, so that these materials can be exploited for their potential applications in magnetic energy transformations [9].

Traditionally, these charming magnetic characteristics arise in spinel structures due to distribution of cations at two distinctive sites, termed as X- and Y-sites [10]. The magnetic moments of cations present at these sites are aligned parallel or partially antiparallel to support net magnetic moment. Hence, the general formula of spinel structure is written as XY_2O_4, in which divalent X (II) ions occupy the tetrahedral voids, whereas the trivalent Y (III) ions occupy the octahedral voids in the closed packed arrangement of oxygen ions. The spinel unit cell has eight face-centered cubic cells which lead to a big structure, having 32 oxygen atoms, eight X-type and 16 Y-type atoms. Based on the distribution of these atoms within the spinel structure, these compounds exhibit lucrative magnetic properties banking on the composition of cations. In other words, based on the X- and Y-site cations, it exhibits ferromagnetic, antiferromagnetic, spin-glass and paramagnetic behaviors [11–13].

For example, in a recent study, cubic spinel-structured XCr_2O_4 (X = Mn or Co) has shown frustrated results in the form of nonlinear spiral magnetic order at temperature below the transition temperature. It is also investigated that the spiral order of polycrystalline $MnCr_2O_4$ is found to be dormant to the exposure of high magnetic field but can be inflected by external pressure [14]. In addition, the electrical properties of these spinel chromites are also tunable and it is investigated that the dielectric constant of $MnCr_2O_4$ is temperature independent, having a value in the range of 2–4, approximately [15]. Magneto-dielectric coupling (MDC) in the polycrystalline samples of $MnCr_2O_4$ has also been reported below the ferromagnetic ordering temperature of 43 K [16]. This MDC could be potentially exploited for future multiferroic devices. Another advantage of $MnCr_2O_4$ is that it offers much better resistance to carbonaceous attack than Cr_2O_3, thus making it preferable for use in industrial high-temperature carbonaceous environments [7].

Conventionally, spinel-structured nanoparticles have been synthesized using a variety of techniques. For instance, Yazdanbakhsh et al. [17] reported the synthesis of nanospinel chromites by thermal decomposition of gel obtained via sol–gel method for the removal of azo-dye

from the aqueous solution. An oxalate decomposition process has been utilized for the preparation of $NiFe_2O_4$ magnetic mesoporous spinel to study its adsorptive property [18]. In addition, the spinel-structured nanoparticles have also been synthesized by assisted co-precipitation [19, 20], spray pyrolysis [21] and solid-state reaction [22].

Although solid-state reaction method is very common for preparing spinels, it requires very high sintering temperatures, often well above 1000 °C for several hours to complete the reaction [23–25]. Other drawbacks of solid-state reaction are inhomogeneity, lack of stoichiometry control and large particle size. In this study, sol–gel-based combustion method is utilized for preparing Cr_2O_3 and $MnCr_2O_4$ nanoparticles to discuss their structural, morphological and magnetic properties, systematically. The reason behind adopting sol–gel-based technique for preparing nanoparticles is high homogeneity, low temperature, controlled shape and size of nano particles [3, 26]. Change in magnetic behavior of Cr_2O_3 nanoparticles due to Mn incorporation and magnetic phase transition temperature of $MnCr_2O_4$ has been determined.

2 Experimental

Cr_2O_3 and $MnCr_2O_4$ samples in powder form were synthesized by sol–gel auto-combustion method. Stoichiometrically weighed appropriate amounts of starting materials, i.e., chromium nitrate [$Cr(NO_3)_3.9H_2O$, Sigma-Aldrich, ≥99.9], manganese nitrate [$Mn(NO_3)_2.4H_2O$, Sigma-Aldrich, ≥99.5] and citric acid [$C_6H_8O_7$, Sigma-Aldrich, ≥99.8], were separately dissolved in deionized (DI) water to earn homogeneous solutions and then mixed together to make 50 mL solution. Initially, the metal nitrates (MN) and citric acid (CA) were weighed using a precision digital balance keeping MN to CA molar ratio of 1:2. The molar ratio of $Mn(NO_3)_2.4H_2O$ to $Cr(NO_3)_3.9$-H_2O, for instance, in the preparation of $MnCr_2O_4$ was taken as 1:2, as well, in accordance with (atomic) moles present in one formula unit of $MnCr_2O_4$. The mixed solution was placed on a hot plate, and the whole setup was transferred to an ESCO fume hood. The mixture was heated and stirred magnetically at 95 °C for about 45 min until sol was formed. The sol was further heated at this temperature to make gel. As the gel was formed, the magnetic stirrer was removed and the temperature of gel was increased in definite intervals up to 350 °C. After a while, the gel was burnt in a suddenly evolved exothermic reaction and the resultant product was a loose, fluffy and homogenously dried powder. The powder was ground to improve homogeneity by an agate mortar and pestle and subsequently sintered at 600 °C for 2 h, in a muffle furnace (Nabertherm P301, Germany), in order to develop desired

crystalline phase. Earlier, stoichiometric proportions of chromium nitrate and citric acid were dissolved in DI water for the preparation of Cr_2O_3 using the same procedure. Afterward, the powder samples were pelletized using an Apex hydraulic press having diameter 10 mm and thickness of 1.2 ± 0.01 mm.

Phase identification and detailed analysis of crystalline structure were performed using Bruker D/8 Advance X-ray diffractometer (XRD). Grain size was determined using elegant images of samples taken by NovaNano 450-SEM field emission scanning electron microscope (FESEM), and the elemental composition was determined using an Oxford Instruments energy-dispersive X-ray spectroscopy (EDX). Low-temperature magnetic measurements were performed using a cryogen-free measurement system (CFMS).

3 Results and discussion

Crystal structure of the samples was identified using XRD in the 2θ range of 20°–80° with Cu-K_α radiation ($\lambda = 1.54$ Å) operated at 30 kV. The XRD pattern of Cr_2O_3, as shown in Fig. 1, reveals that all the diffracted peaks belong to rhombohedral crystal structure having space group R-3c, as the peaks were perfectly matched with ICSD file No. 00-038-1479, a characteristics reference pattern of Cr_2O_3. No impurity peaks were evident in the pattern.

Figure 2 exhibits the XRD pattern of $MnCr_2O_4$. The pattern was indexed following the procedure as described by Cullity [27]. Data retrieved from diffraction were plotted, and intensity peaks were identified. Peak positions helped to find $\sin^2\theta$ values and subsequently using the relation, $\sin^2\theta \propto h^2 + k^2 + l^2$, hkl values were assigned to the diffracted peaks. The proportionality indicates that planes with lager values of diffraction angles have higher miller indices. The indexed diffracted peaks corresponding to the planes (220), (311), (222), (400), (511) and (440)
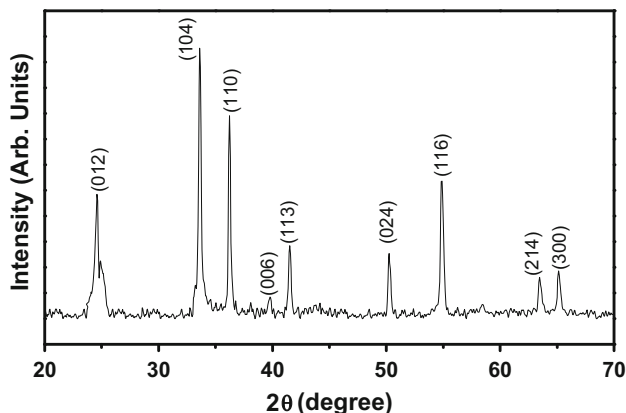

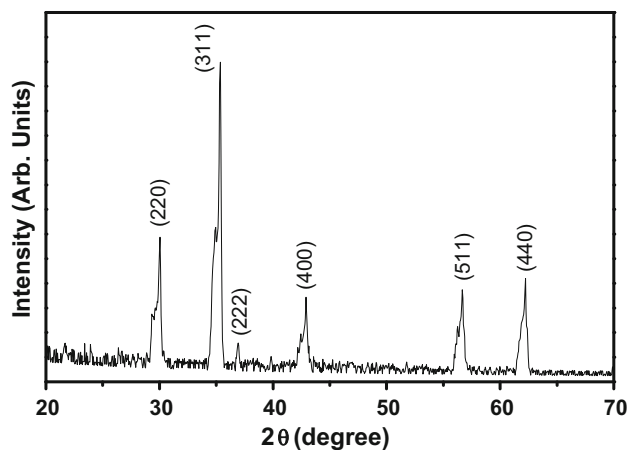Fig. 1 XRD pattern of Cr_2O_3 sintered at 600 °C for 2 h

Fig. 2 XRD pattern of $MnCr_2O_4$ sintered at 600 °C for 2 h

elaborated that the crystal structure of $MnCr_2O_4$ is spinel cubic with space group $Fd3\ m$. It revealed that phase pure $MnCr_2O_4$ was obtained as no peaks related to any impurity phase were found. Lattice parameters were determined using the relation, $a = \lambda\sqrt{h^2 + k^2 + l^2}/2\mathrm{Sin}\theta$, where λ was the wavelength of X-rays. The indexed pattern was also matched well with ICSD file No. 01-075-1614, a reference pattern of $MnCr_2O_4$, with cubic spinel structure. Hence, the evaluated structural parameters were confirmed. Crystallite size of Cr_2O_3 and $MnCr_2O_4$ samples was determined using Scherrer's formula, $D = 0.9\lambda/\beta\mathrm{Cos}\theta$ where D, λ, β and θ were the average crystallite size, X-ray wavelength, full width at half maximum (FWHM) in radians and the Bragg's angle in degrees, respectively. Other structural parameters, such as volume of unit cell (V), bulk density ($\rho_b = m/\pi r^2 h$, where m is mass, r is radius and h is thickness of the pellet samples), X-ray density ($\rho_x = 2\ M/N_A V$, where M is molar mass and N_A is Avogadro's number) and porosity ($P = 1 - \rho_b/\rho_x$) of both the samples, were also evaluated. The calculated values of all these parameters are shown in Table 1.

Figure 3 shows FESEM images of both the samples obtained at different magnifications. Figure 3a, b exhibits the structural morphology of Cr_2O_3 sample which reveals finely dispersed, well-defined grains with sharp grain boundaries, which are mostly spherical in shape and distributed homogenously. Mostly the particles are well separated from each other; however, few agglomerations of grain clusters are also observed. Dark voids represent the porosity of the samples which is estimated well in agreement, as determined from the diffraction data. The average particle size as evaluated using the software Image J is 35 ± 5 nm for Cr_2O_3. Figure 3c, d exhibits the structural morphology of $MnCr_2O_4$ at different magnifications. In this case, the individual nanoparticles are also well defined with sharp boundaries. However, the size of nanoparticles is

Table 1 Lattice constant, crystallite size, unit cell volume, bulk density, X-ray density and porosity of Cr_2O_3 and $MnCr_2O_4$ nanoparticles

Sample	Lattice constant (Å)	Crystallite size D (nm)	Unit cell volume (Å^3)	Bulk density, ρ_b (g/cm^3)	X-ray density, ρ_x (g/cm^3)	Porosity (%)
Cr_2O_3	$a = b = 4.9588$ $c = 13.5942$	31.96	289	2.87	5.24	45
$MnCr_2O_4$	$a = b = c = 8.4606$	32.03	605	2.10	4.89	57

Fig. 3 FESEM images of Cr_2O_3 at **a** 100,000×, **b** 300,000×, and $MnCr_2O_4$ at (c) 100,000× and (d) 300,000× magnification
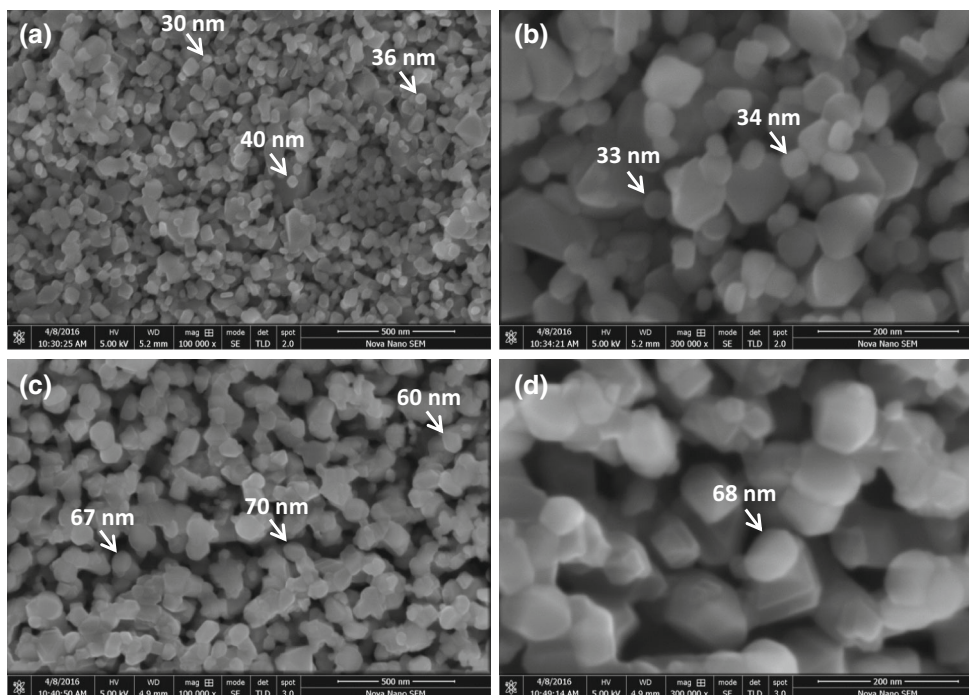
increased and determined as 65 ± 5 nm. Careful look at magnified image reveals sharp faces of crystalline particles. Density of black spots is also increased contributing more toward porosity.

Size and distribution of hydrodynamic diameter of synthesized powder samples was determined using dynamic light scattering (DLS), as shown in Fig. 4. DLS measures the hydrodynamic diameter of particle which is always larger than the particle size as determined using high resolution (HR) microscopic techniques. This is due to the fact that in hydrodynamic measurements, surfactant or solvent layers adhere to the surrounding of the particle, thus enlarging it as compared to its parent size. The importance of this measurement is that it provides suitability of nanoparticles in biological environments [28]. In DLS, light scatters at different angles after striking with suspended particles in the solution. The scattered light interferes and is detected by light detectors. The interference patterns of light change continuously due to Brownian motion of the particles. In this way, DLS gives information about the size range of particles from minimum to
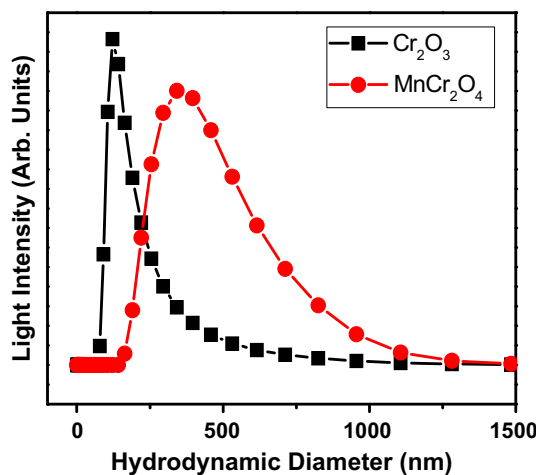

Fig. 4 DLS plots of Cr_2O_3 and $MnCr_2O_4$ samples

maximum as shown in Fig. 4. Maximum hydrodynamic size of the Cr_2O_3 particles was observed as 120 and 350 nm for $MnCr_2O_4$.

Stoichiometric elemental composition and purity of prepared samples were further confirmed by EDX analysis. The EDX spectra shown in Fig. 5a reveals intensity peaks related to only Cr and O. This confirms the synthesis of impurity-free Cr_2O_3, as no other element is detected. In Fig. 5b, peaks corresponding to Mn are also observed in addition to Cr and O. This confirms the phase pure synthesis of $MnCr_2O_4$. The at% and wt% of all the elements, as shown in Table 2, are in strict accordance with the stoichiometric composition of these elements in their respective formula units.

Magnetic properties of Cr_2O_3 and $MnCr_2O_4$ nanoparticles were determined using CFMS. Conventionally, magnetic characteristics of magnetic nanomaterials depend on elemental composition, lattice parameters, particle size, order of applied field, etc. [29]. Antiferromagnetic materials when reduced to nanoscale, for instance in the form of ultra-thin layers or discrete particles, exhibit weak ferromagnetism. This characteristic behavior normally increases with decreasing particle size [30]. Figure 6 shows the magnetic hysteresis (M–H) loops of Cr_2O_3, measured at 5 and 300 K. It can be seen that sample presents a paramagnetic behavior both at room temperature and at 5 K, although bulk Cr_2O_3 is antiferromagnetic [31]. The magnetization curves are essentially linear up to approximately 5 T without any tendency toward saturation. However, at 5 K, the M–H loop shows a minute indication of remanence as shown in inset of Fig. 6. The reason is that, at

Table 2 Quantitative data of wt% and at% of all the elements in Cr_2O_3 and $MnCr_2O_4$ samples

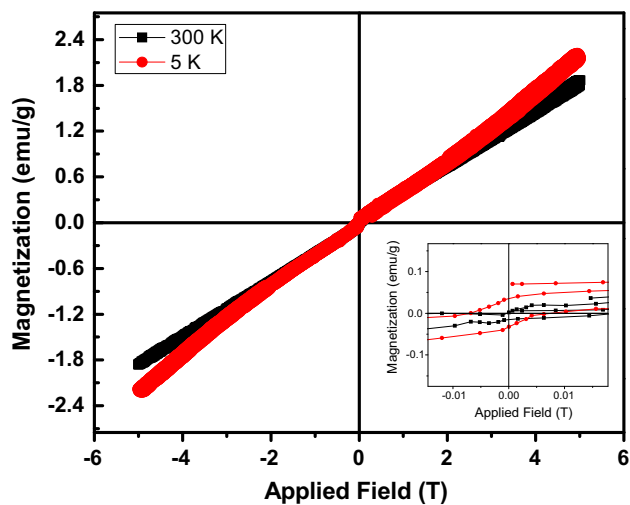| Element	wt%	at%	Element	wt%	at%
Cr	65.15	38.06	Mn	23.14	13.07
O	34.85	61.94	Cr	45.29	36.19
…	…		O	31.57	16.00
Total	100	100		100	100

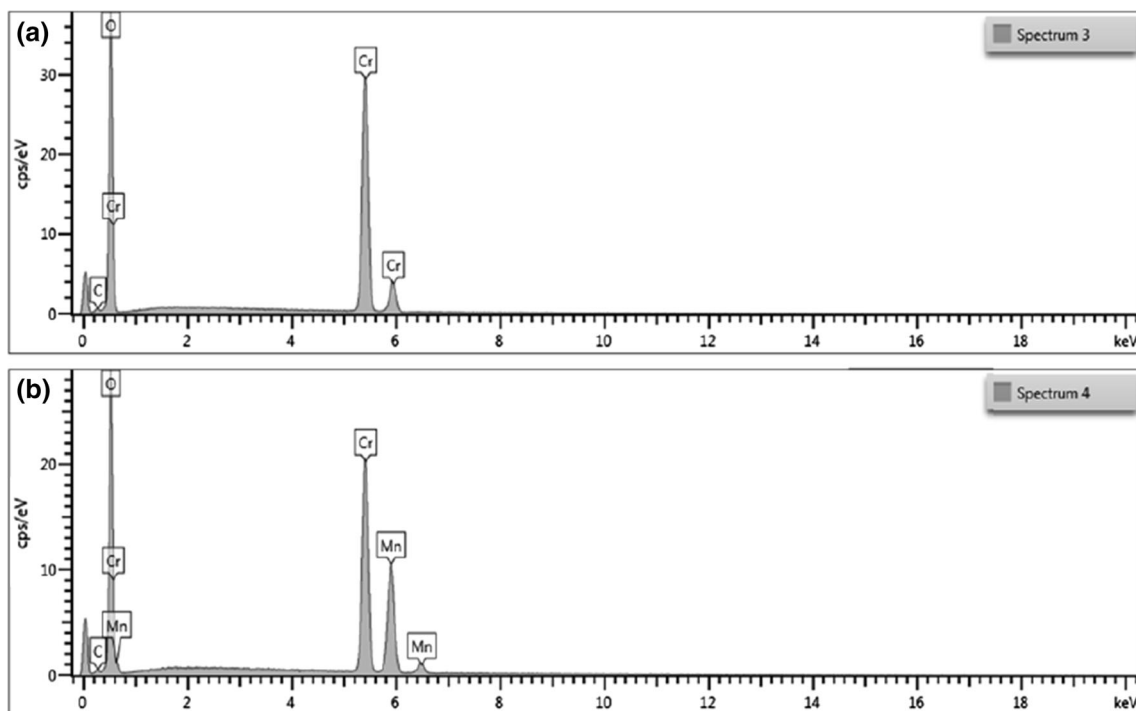**Fig. 6** Magnetic hysteresis (M–H) loops of Cr_2O_3 at 300 and 5 K

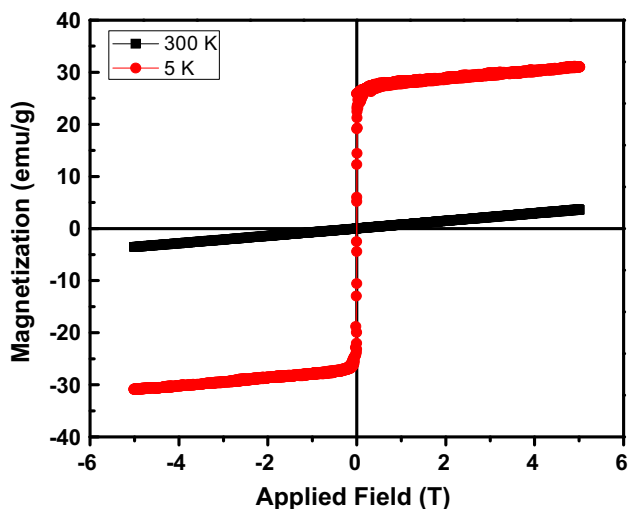**Fig. 5** EDX spectra of **a** Cr_2O_3 and **b** $MnCr_2O_4$ samples

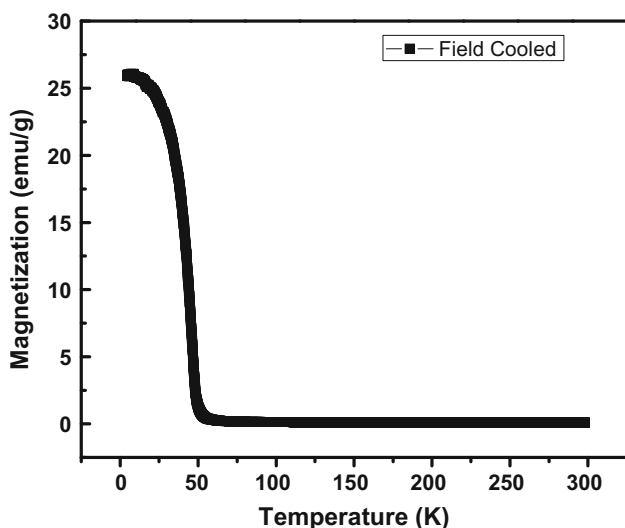**Fig. 7** Magnetic hysteresis (M–H) loops of $MnCr_2O_4$ at 300 and 5 K

Fig. 8 Magnetization versus temperature plot of $MnCr_2O_4$ under field-cooled condition

very low temperature such as 5 K, the disordering effect of thermal agitation is suppressed by aligning tendency of magnetic moments, which leads to a large value of the Langvin variable ($a = \mu H/kT$). Besides this, earlier studies have reported that Cr_2O_3 exhibits weak ferromagnetic behavior in ultra-thin films or discrete particles [32, 33].

On the other hand, $MnCr_2O_4$ also exhibits paramagnetic behavior at room temperature (300 K) due to partly aligned magnetic moments in the direction of applied field, but present a ferromagnetic behavior at 5 K, as shown in Fig. 7. As temperature is decreased, maximum number of magnetic moments interact with each other according to Curie–Weiss Law ($\chi = C/T - \theta$) and orient themselves in the direction of applied field. Furthermore, according to

Langvin theory, at low temperature or at high applied magnetic field (H) saturation occurs due to large value of Langvin function ($M/M_0 = L(a)$). Therefore, in the consequences of Langvin theory, the loop is saturated at 5 K (Fig. 7) and estimated value of remanence is 26.39 emu/g. Figure 8 shows temperature-dependent field cold (FC) magnetic behavior of $MnCr_2O_4$ obtained at an applied filed of 1 T. The Curie temperature (T_c) of $MnCr_2O_4$, defined by the maxima of $-dM/dT$ of FC curves [34], leading to the ferromagnetic transition is determined as 50 K. This value of T_c is comparable with already reported values of T_c for $MnCr_2O_4$, which vary between 41 and 55 K [11, 34, 35]. With a decrease in temperature below T_c, FC curve shows kink-like anomaly around 50 K.

4 Conclusion

In this study, Cr_2O_3 and $MnCr_2O_4$ nanoparticles have been successfully synthesized via sol–gel auto-combustion technique using citric acid as a fuel. This proposed method has the important advantage of being simple, fast and cost effective. XRD revealed a structural transformation from rhombohedral (Cr_2O_3) to cubic spinel ($MnCr_2O_4$), when Mn is incorporated in Cr_2O_3. Finely dispersed and symmetrically distributed grains were revealed by FESEM having average sizes as 55 ± 5 and 60 ± 5 nm, for Cr_2O_3 and $MnCr_2O_4$, respectively. EDX spectra confirmed the impurity-free composition of both the samples. Hydrodynamic radii of particles of both the samples were determined using dynamic light scattering. Magnetic characterizations revealed that synthesized Cr_2O_3 nanoparticles possess paramagnetic characteristics both at room temperature and at 5 K. On the other hand, ferromagnetic transition at 50 K was observed in $MnCr_2O_4$.

References

1. Sun B, Wu J, Jia X, Lou F, Chen P (2015) Preparation and light-controlled resistive switching memory behavior of $CuCr_2O_4$. J Sol-Gel Sci Technol 75:664–669
2. Saha D, Giri R, Mistry KK, Sengupta K (2005) Magnesium chromate–TiO_2 spinel tape cast thick film as humidity sensor. Sens Actuators B Chem 107:323–331
3. Geng Q, Zhao X, Gao X, Yang S, Liu G (2012) Low-temperature combustion synthesis of $CuCr_2O_4$ spinel powder for spectrally selective paints. J Sol-Gel Sci Technol 61:281–288
4. Paul B, Bhuyan B, Purkayastha DD, Dhar SS, Behera S (2015) Facile synthesis of spinel $CuCr_2O_4$ nanoparticles and studies of

their photo catalytic activity in degradation of some selected organic dyes. J Alloys Compd 648:629–635

5. Ahmad SS, Rhamdhani M, Pownceby M, Bruckard W (2016) Selective sulfidising roasting for the removal of chrome spinel impurities from weathered ilmenite ore. Int J Miner Process 146:29–37

6. Kim D, Lhm S (2001) Application of spinel-type cobalt chromite as a novel catalyst for combustion of chlorinated organic pollutants. Environ Sci Technol 35:222–226

7. Li H, Chen W (2010) Stability of $MnCr_2O_4$ spinel and Cr_2O_3 in high temperature carbonaceous environments with varied oxygen partial pressures. Corros Sci 52:2481–2488

8. Lau K, Kandalam A, Costales A, Pandey R (2004) Equilibrium geometry and electron detachment energies of anionic Cr_2O_4, Cr_2O_5, and Cr_2O_6 clusters. Chem Phys Lett 393:112–117

9. Jankovsky O, Sedmidubsky D, Sofer Z, Luxa J, Bartunek V (2015) Simple synthesis of Cr_2O_3 nanoparticles with a tunable particle size. Ceram Int 41:4644–4650

10. Tong J, Cai X, Wang H, Xia C (2013) Efficient magnetic $CoFe_2O_4$ nanocrystal catalyst for aerobic oxidation of cyclohexane prepared by sol–gel auto-combustion method: effects of catalyst preparation parameters. J Sol-Gel Sci Technol 66:452–459

11. Masrour R, Hamedoun M, Benyoussef A (2010) Magnetic properties of $MnCr_2O_4$ nanoparticle. J Magn Magn Mater 322:301–304

12. Peelamedu R, Grimes C, Agrawal D, Roy R, Yadoji P (2003) Ultralow dielectric constant nickel–zinc ferrites using microwave sintering. J Mater Res 18:2292–2295

13. Hossain AKMA, Seki M, Kawai T, Tabata H (2004) Colossal magneto resistance in spinel type $Zn_{1-x}Ni_xFe_2O_4$. J Appl Phys 96:1273–1275

14. Zhou Y, Yang Z, Li L, Xie Y, Lin S, Sun Y, Zhang Y (2012) Magnetic field and external pressure effects on the spiral order of polycrystalline $MnCr_2O_4$. J Magn Magn Mater 324:3799–3801

15. Song S, Yuan Z (2003) Electrical properties of $MnCr_2O_4$ spinel. J Mater Sci Lett 22:755–757

16. Mufti N, Blake GR, Palstra TTM (2009) Magneto dielectric coupling in $MnCr_2O_4$ spinel. J Magn Magn Mater 321:1767–1769

17. Yazdanbakhsha M, Khosravi I, Goharshadi G, Youssefi A (2010) Fabrication of nano spinel $ZnCr_2O_4$ using sol–gel method and its application on removal of azo dye from aqueous solution. J Hazard Mater 184:684–689

18. Gao Z, Cui F, Zeng S, Guo L, Shi J (2010) A high surface area super paramagnetic mesoporous spinel ferrite synthesized by a template-free approach and its adsorptive property. Microporous Mesoporous Mater 132:188–195

19. Sivakumar P, Ramesh R, Ramanand A, Ponnusamy S, Muthamizhchelvan C (2013) Synthesis and characterization of $NiFe_2O_4$ nanoparticles and nanorods. J Alloys Compd 563:6–11

20. Matulkova I, Holec P, Pacakova B, Kubickova S, Mantlikova A, Plocek J, Nemec I, Niznansky D, Vejpravova J (2015) On preparation of nano crystalline chromites by co-precipitation and autocombustion methods. Mater Sci Eng B 195:66–73

21. Marinkovic Z, Mancic L, Maric R, Milosevic O (2001) Preparation of nanostructure Zn–Cr–O spinel powders by ultrasonic spray pyrolysis. J Eur Ceram Soc 21:2051–2055

22. Levy S, Diella D, Pavese V, Dapiaggi A, Sani M (2005) P-V equation of state, thermal expansion and P–T stability of synthetic ($ZnCr_2O4$ spinel). Am Miner 90:1157–1167

23. Hilczer A, Kowalska K, Markiewicz E, Pietraszko A, Andrzejewski B (2016) Dielectric and magnetic response of $SrFe_{12}O_{19}$–$CoFe_2O_4$ composites obtained by solid state reaction. Mater Sci Eng B Solid 207:47–55

24. Marinkovic ZV, Mancic L, Vulic P, Milosevi O (2005) Microstructure characterization of mechanically activated ZnO–Cr_2O_3 system. J Eur Ceram Soc 25:2081–2093

25. Bayhan M, Hashemi T, Brinkman A (1997) Sintering and humidity-sensitive behavior of the $ZnCr_2O_4$–K_2CrO_4 ceramic system. J Mater Sci 32:6619–6623

26. Ghafoor I, Siddiqi SA, Atiq S, Riaz S, Naseem S (2015) Sol–gel synthesis and investigation of structural, electrical and magnetic properties of Pb doped $La_{0.1}Bi_{0.9}FeO_3$ multiferroics. J Sol-Gel Sci Technol 74:352–356

27. Cullity BD (1977) Elements of X-ray diffraction, 2nd edn. Notre Dame

28. Carvalho JWJ, Carvalho FAO, Batista T, Santiago PS, Tabak M (2014) Cetyltrimethylammonium chloride (CTAC) effect on the thermal stability of oxy-HbGp: dynamic light scattering (DLS) and small angle X-ray scattering (SAXS) studies. Colloid Surf B 118:14–24

29. Sobhani A, Niasari M (2013) Synthesis, characterization, optical and magnetic properties of a nickel sulfide series by three different methods. Superlattices Microstruct 59:1–12

30. Anandan K, Rajendran V (2014) Studies on structural, morphological, magnetic and optical properties of chromium sesquioxide (Cr_2O_3) nanoparticles: synthesized via facile solvo thermal process by different solvents. Mat Sci Semicon Process 19:136–144

31. Vollath D, Szabo D, Willis J (1996) Magnetic properties of nano crystalline Cr_2O_3 synthesized in a microwave plasma. Mater Lett 29:271–279

32. Pokhrel S, Simion C, Quemener V, Barsan N, Weimar U (2008) Investigations of conduction mechanism in Cr_2O_3 gas sensing thick films by ac impedance spectroscopy and work function changes measurements. Sens Actuators B Chem 133:78–83

33. Zhang W, Bru E, Zhang Z, Tegus O, Li W, Si P, Geng D, Buschow K (2005) Structure and magnetic properties of Cr nanoparticles and Cr_2O_3 nanoparticles. Phys B 358:332–338

34. Jhuang YC, Kuo KM, Chern G (2011) Structural and magnetic characterizations of Mn_2CrO_4 and $MnCr_2O_4$ films on MgO(001) and SrTiO3(001) substrates by molecular beam epitaxy. J Appl Phys 109:07D714

35. Hastings JM, Corliss LM (1962) Magnetic structure of manganese chromite. Phys Rev 126:556–565